

# Drifting Electrons: Nonreciprocal Plasmonics and Thermal Photonics

S. ALI HASSANI GANGARAJ,<sup>1,†</sup> FRANCESCO MONTICONE,<sup>1,\*</sup>

<sup>1</sup>*School of Electrical and Computer Engineering, Cornell University, Ithaca, NY, 14853, USA*

<sup>†</sup>*ali.gangaraj@gmail.com*

<sup>\*</sup>*francesco.monticone@cornell.edu*

**Abstract:** Light propagates symmetrically in opposite directions in most materials and structures. This fact – a consequence of the Lorentz reciprocity principle – has tremendous implications for science and technology across the electromagnetic spectrum. Here, we investigate an emerging approach to break reciprocity that does not rely on magneto-optical effects or spacetime modulations, but is instead based on biasing a plasmonic material with a direct electric current. Using a 3D Green function formalism and microscopic considerations, we elucidate the propagation properties of surface plasmon-polaritons (SPPs) supported by a generic nonreciprocal platform of this type, revealing some previously overlooked, anomalous, wave-propagation effects. We show that SPPs can propagate in the form of steerable, slow-light, unidirectional beams associated with inflexion points in the modal dispersion. We also clarify the impact of dissipation (due to collisions and Landau damping) on nonreciprocal effects and shed light on the connections between inflexion points, exceptional points at band edges, and modal transitions in leaky-wave structures. We then apply these concepts to the important area of thermal photonics, and provide the first theoretical demonstration of drift-induced nonreciprocal radiative heat transfer between two planar bodies. Our findings may open new opportunities toward the development of nonreciprocal magnet-free devices that combine the benefits of plasmonics and nonreciprocal photonics for wave-guiding and energy applications.

© 2022 Optical Society of America under the terms of the [OSA Open Access Publishing Agreement](#)

## 1. Introduction

The Lorentz reciprocity principle limits the performance of electromagnetic and photonic devices in a wide range of areas, from communication systems to quantum computing and thermal photonics. A reciprocal system, with its symmetric response when source and detector are interchanged, is not ideal when classical/quantum energy/information needs to be emitted, transferred, and absorbed unidirectionally with high efficiency, or when different information streams need to be selectively routed or processed based on their propagation direction. Standard nonreciprocal devices, such as magneto-optical isolators or circulators, are routinely used in many of these scenarios, but with the increasing demand for efficient electromagnetic and photonic integrated systems, there has been increasing interest in different solutions that permit asymmetric or, in the extreme case, truly unidirectional and beam-like wave propagation at small scales. In this context, particularly intriguing opportunities may be offered by combining the benefits of plasmonics (field localization and enhancement) with strong nonreciprocal effects [1].

The oldest and most common approach to break reciprocity and achieve one-way light propagation is based on the magneto-optical effect, which requires biasing certain materials (plasmas, ferrites, magnetic garnets, etc.) with a static magnetic field [2–15]. However, the need for a large external magnet, the weakness of the magneto-optical response at the relevant frequencies, and other practical issues, make this approach less appealing to realize strong nonreciprocal effects at the (sub)wavelength scale and for on-chip integration. Other approaches to break reciprocity have been extensively studied in the recent past, relying on nonlinear phenomena [16–22], spatiotemporal modulations [23–25], and multi-physics, e.g.,

46 optomechanical, interactions [26–28]. Unfortunately, however, the issues associated with  
47 dynamic reciprocity for nonlinear nonreciprocal devices, the typically narrowband response  
48 of optomechanical resonators, and the practical difficulties in implementing spatiotemporal  
49 modulations at high frequencies limit the applicability of these approaches.

50 In addition to unidirectional wave-guiding, another particularly important area that may benefit  
51 from strong forms of nonreciprocity is thermal photonics [30]. According to Kirchhoff’s law  
52 of thermal radiation, the emissivity of a material is exactly equal to its absorptivity, at each  
53 frequency and angle. Rather remarkably, this law is not a consequence of the Second Law of  
54 Thermodynamics, but it originates directly from Lorentz reciprocity [29–31] and is analogous to  
55 other relevant symmetries in electromagnetics, such as the fact that antennas made of reciprocal  
56 materials can be used in reception and transmission with exactly the same gain and directivity.  
57 One of the direct consequences of reciprocity in this context is that an efficient absorber will also  
58 be an efficient emitter. For instance, an absorber designed to efficiently harvest solar radiation must  
59 radiate part of the energy back to the environment, which represents an intrinsic loss mechanism.  
60 This is the idea behind the Landsberg limit [32], which sets the upper efficiency bound for  
61 harvesting incoming solar radiation. This limit can only be reached with the use of nonreciprocal  
62 systems [32–35]. Moreover, breaking the symmetry between absorptivity and emissivity may  
63 also open new opportunities for near-field heat transfer. Nonreciprocal systems have been shown  
64 to enable thermal Hall effects [36] and the emergence of persistent heat currents in systems in  
65 thermal equilibrium at a certain temperature (analogous to persistent electrical or mass currents  
66 in superconductors or superfluids, respectively) [37]. Such nonreciprocal systems may become  
67 an important element in the quest for controlling heat flow at the nanoscale with large flexibility  
68 and efficiency. As in the case of nonreciprocal wave-guiding, nonreciprocal effects in thermal  
69 photonics are typically obtained by relying on magneto-optical materials [31, 33, 38–41], which  
70 have been theoretically shown to enable a near-complete violation of Kirchhoff’s law [39, 40]  
71 or nonreciprocal heat transfer between planar bodies [38]. Again, due to the weakness of  
72 magneto-optical effects at optical frequencies, these platforms require a relatively strong magnetic  
73 bias, which may raise questions about their practical applicability. A relevant exception is  
74 Ref. [42], where nonreciprocal emission/absorption was realized using space-time modulations;  
75 this strategy, however, was only demonstrated at microwave frequencies, in the form of a  
76 nonreciprocal leaky-wave antenna, and applying it to optical frequencies involves significant  
77 challenges.

78 In contrast with these previous studies, here we focus on a drastically different approach to  
79 break reciprocity in plasmonic platforms without the need for magneto-optical or dynamical  
80 effects. This approach is based on biasing certain conducting materials with a direct electric  
81 current, which, just like the magnetic field, is a quantity that is odd under time reversal and,  
82 therefore, it can be used to break reciprocity [29]. This strategy can in principle be applied to  
83 either three-dimensional (3D) conducting materials (metals, degenerately doped semiconductors,  
84 and plasmas) or two-dimensional (2D) media such as graphene, and it has been the subject  
85 of increasing attention in the plasmonic literature [43–53], with a very recent experimental  
86 demonstration at optical frequencies [54]. Strong nonreciprocal effects emerge if the electron  
87 drift velocity  $v_d$  is large enough to affect the dispersion of surface plasmon-polaritons (SPPs),  
88 which is possible in certain high-mobility conducting materials (e.g., graphene). The effect of  
89 drifting electrons on SPP propagation can be qualitatively explained in an intuitive way: surface  
90 waves on plasmonic materials involve collective charge oscillations coupled to electromagnetic  
91 fields; these propagating waves are dragged or opposed by the drifting electrons, which implies  
92 that SPPs “see” different media when propagating along or against the current flow. In other  
93 words, it was argued in [47] that, in a current-biased 3D plasmonic medium, the drifting electrons  
94 produce a Doppler shift in the isotropic material permittivity, i.e.,  $\omega \rightarrow \omega - \mathbf{k} \cdot \mathbf{v}_d$ , where  $\mathbf{k}$  is  
95 the wavevector. Such a linear wavevector-dependence implies that the material response becomes

96 nonlocal (spatially dispersive), as well as nonreciprocal since oppositely propagating waves see  
 97 a different permittivity. In Section 2, we clarify that, even though this Doppler-shift argument  
 98 is strictly valid only for longitudinal modes (in general, the permittivity becomes a spatially  
 99 dispersive tensor [55]), under certain conditions it provides a good approximation of the exact  
 100 results and allows for a drastic simplification of the analysis and simulations.

101 While all previous works on drift-induced nonreciprocity were mostly interested in the 1D  
 102 problem of one-way SPP propagation along the current flow or on specific 2D materials such as  
 103 graphene, here, in the first part of the paper, we use a 3D Green function formalism to elucidate  
 104 the different regimes of nonreciprocal SPP propagation on the 2D surface of a generic 3D  
 105 plasmonic platform, revealing a number of anomalous and extreme wave-propagation effects  
 106 beyond unidirectional propagation. We also clarify how the unavoidable presence of losses in this  
 107 plasmonic platform affects the nonreciprocal modal dispersion. Then, in the second part of this  
 108 work, we investigate, for the first time to the best of our knowledge, the potential of current-biased  
 109 nonreciprocal systems for thermal photonics, and we theoretically demonstrate a clear signature  
 110 of drift-induced nonreciprocity in the canonical problem of radiative heat-transfer between two  
 111 planar bodies.

## 112 2. Current-Induced Nonreciprocity in Three-Dimensional Plasmonic Platforms

113 We consider the general problem of SPP propagation along a planar metallic-dielectric interface  
 114 at  $z = 0$ , as shown in Fig. 1(a). We employ a 3D Green function analysis (see Supplemental  
 115 Material) to study both the dispersion properties of the supported SPP eigenmodes and their  
 116 propagation properties in source-excited configurations, for both local (non-biased, reciprocal)  
 117 and nonlocal (current-biased, nonreciprocal) plasmonic materials. We assume a laterally infinite  
 118 interface between two different materials with permittivity  $\epsilon_1$  for  $z < 0$  and  $\epsilon_2$  for  $z > 0$   
 119 (permeability  $\mu_1 = \mu_2 = \mu_0$ ), and source/observation point above the interface (Fig. 1(a)).

120 For the transparent dielectric region we consider vacuum and for the metallic/plasmonic region,  
 121 in the local non-biased case, we employ a standard Drude model for a free-electron gas with  
 122 permittivity  $\epsilon(\omega) = 1 - \omega_p^2(1 + i\Gamma/\omega)/(\omega + i\Gamma)^2$ , where  $\omega_p$  is the plasma frequency and  $\Gamma$  is the  
 123 damping rate. In the following, we first study the problem with  $\Gamma = 0$  (lossless case), whereas the  
 124 impact of dissipation is discussed in details in Section 2.3. At a local, isotropic, metal-vacuum  
 125 interface, SPPs are known to exist for frequencies  $\omega \leq \omega_{SPP} = \omega_p/\sqrt{2}$ . The 3D dispersion  
 126 surface of these SPP eigenmodes, calculated by tracking the poles of the Green function integrand  
 127 in Eq. (33) of the Supplemental Material, is shown in Fig. 1(b) for the lossless case. The  
 128 dispersion surface clearly exhibits a flat dispersion asymptote at the surface plasmon resonance  
 129  $\omega = \omega_{SPP}$ , as expected for a local/lossless Drude model [56] (see, e.g., [1, 8] and references  
 130 therein, for a discussion of how losses and nonlocal effects modify this dispersion diagram).  
 131 The rotationally symmetric shape of the dispersion surface with respect to in-plane wavevectors  
 132 indicates that the surface mode propagates reciprocally and isotropically on the interface. The  
 133 spatial field distribution of the SPPs excited by a vertically polarized source as in Fig. 1(a) was  
 134 calculated using our 3D Green function formalism at  $\omega = 0.6\omega_p$  (see Fig. 1(d)), confirming that  
 135 surface waves propagate symmetrically and omnidirectionally along the interface.

136 As discussed in Ref. [1], strong nonreciprocity and unidirectionality in a continuous plasmonic  
 137 platform of this type can be achieved if the mechanism that breaks reciprocity introduces an  
 138 asymmetry in the dispersion asymptote for large wavevectors. While this is typically achieved  
 139 with a static magnetic bias, a direct current bias, which can be directly carried by plasmonic  
 140 materials due to their conductive nature, can also introduce a strong asymmetry, but with  
 141 qualitatively different characteristics, as originally discussed in [47]. The presence of a DC current  
 142 means that conduction electrons move with average drift velocity  $v_d = J_0/ne$  where  $J_0$  is the  
 143 current density,  $n = m\omega_p^2/4\pi e^2$  is the electron density, and  $e$  is the negative electron charge.  
 144 Ref. [47] argues that the movement of electrons produces a Doppler frequency shift in the

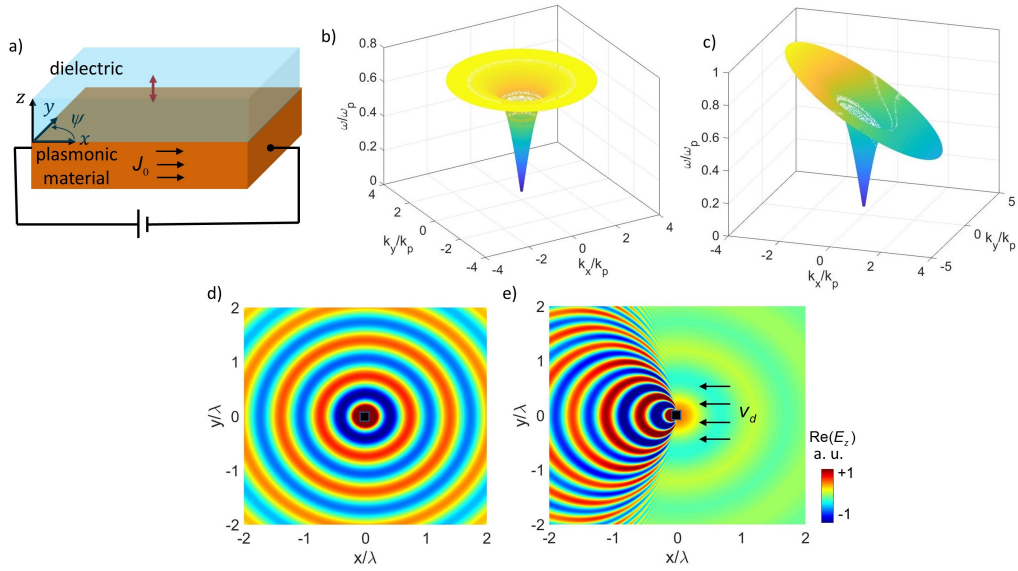


Fig. 1. (a) Geometry under consideration: a plasmonic material is interfaced with a transparent dielectric. A vertically polarized point dipole source radiates close to the interface in the dielectric region. The supported SPP dispersion surface is shown in (b) for a reciprocal isotropic plasmonic material, with no current bias, interfaced with free space, and (c) for the same configuration but with the plasmonic material biased by a direct current with drift velocity  $\mathbf{v}_d = -c/10\hat{x}$ . (d,e) Source-excited in-plane distribution of the SPP electric field (time snapshot of the  $z$  component) in the reciprocal and nonreciprocal cases: (d) without DC current at frequency  $\omega/\omega_p = 0.6$ , and (e) with DC current at  $\omega/\omega_p = 0.8$ . For panels (d) and (e) the source is located at  $z_0 = \lambda/10$  above the interface, where  $\lambda$  is the free-space wavelength at the radiation frequency. The black square at the center denotes the source position. Animations of the calculated time-harmonic electric field distribution, for the reciprocal and nonreciprocal cases, are included as Supplemental Material.

145 material permittivity, i.e.,  $\epsilon(\omega - \mathbf{k} \cdot \mathbf{v}_d) = 1 - \omega_p^2 / (\omega - \mathbf{k} \cdot \mathbf{v}_d)^2$ , such that the material response  
 146 becomes spatially dispersive, with a wavevector-dependent isotropic permittivity. This point, and  
 147 especially the isotropy assumption, is worth some clarification. As discussed in [55, 60], in the  
 148 presence of any non-trivial electron velocity distribution (due to a current bias or just the thermal  
 149 motion of free electrons), the permittivity of a free-electron gas becomes spatially dispersive (in  
 150 other words, the material response is nonlocal due to the electrons moving a certain distance  
 151 during one period of the applied electromagnetic field). Importantly, in the presence of spatial  
 152 dispersion, the material permittivity is a tensor even in an isotropic medium. The general form of  
 153 this wavevector-dependent permittivity tensor can be written (in tensor notation in an arbitrary  
 154 coordinate system) as [55],

$$\epsilon_{ij}(\omega, \mathbf{k}) = \epsilon_T(\omega, \mathbf{k}) \left( \delta_{ij} - k_i k_j / k^2 \right) + \epsilon_L(\omega, \mathbf{k}) k_i k_j / k^2 \quad (1)$$

155 where the scalar functions  $\epsilon_T$  and  $\epsilon_L$  are the transverse and longitudinal permittivities (for electric  
 156 fields orthogonal or parallel to  $\mathbf{k}$ , respectively),  $k$  is the wavevector magnitude,  $k_i k_j$  denotes  
 157 a tensor product between the wavevector and itself, and  $\delta_{ij}$  indicates the identity matrix. In  
 158 Supplemental Material (Notes I and II), we derive  $\epsilon_T$  and  $\epsilon_L$  starting from the Vlasov equation  
 159 for plasmas, and we show that only the longitudinal permittivity is perfectly Doppler-shifted in  
 160 the presence of a drift current, whereas the transverse permittivity exhibits a different, weaker

161 form of spatial dispersion. Since the electric field of a SPP mode on a 3D plasmonic material has  
 162 both transverse and longitudinal components inside the material, its dispersion and propagation  
 163 properties are expected to depend on both  $\epsilon_T$  and  $\epsilon_L$ . (in a 2D electron gas, instead, it is clear  
 164 that only the longitudinal conductivity is relevant even if the field has a transverse out-of-plane  
 165 component). This implies that the modeling approach proposed in [47], which uses the same  
 166 equation for SPP dispersion as in the local unbiased case, but substituting the longitudinal  
 167 Doppler-shifted permittivity, can only be approximately valid. To clarify this point, in the  
 168 Supplemental Material (Note I), we derive the exact modal solution for SPPs propagating  
 169 along the electron current and compare it against the SPP dispersion obtained when only the  
 170 longitudinal or transverse permittivity is considered. Our findings show that, while one has to be  
 171 aware of this issue for more accurate calculations, the model proposed in [47] using only the  
 172 longitudinal permittivity is approximately correct and captures the relevant physics especially in  
 173 the large-wavevector regime. Based on these considerations, we can therefore safely use this  
 174 approximate model to drastically simplify the analysis and numerical calculations, and provide  
 175 additional physical insight. Furthermore, it should be mentioned that, while the nonlocal model  
 176 based on the Doppler effect is qualitatively valid for the 3D plasmonic materials considered here,  
 177 its validity for 2D systems, such as graphene, has been the subject of debate in the literature [57],  
 178 and alternative models have been proposed in [43–45, 49, 58]. However, it has been argued that,  
 179 even for 2D systems, this model is accurate when the electron-electron collisions predominate and  
 180 force the electron gas to move with approximately constant velocity, which makes the drift-biased  
 181 medium act similarly to a moving medium [52, 59].

182 While Ref. [47] focused on 1D propagation in the direction of the current, here we use our  
 183 3D Green function formalism to investigate drift-induced nonreciprocal effects over the entire  
 184 two-dimensional interface of the three-dimensional geometry in Fig. 1(a), revealing anomalous  
 185 and extreme forms of surface-wave propagation on this surface. The modified dispersion and  
 186 propagation properties of the SPPs supported by this nonreciprocal configuration can be readily  
 187 analyzed using the same 3D Green function as for the reciprocal case, but, as explained above,  
 188 with the nonlocal, Doppler shifted, longitudinal permittivity,  $\epsilon_L(\omega, \mathbf{k}) = 1 - \omega_p^2 / (\omega - \mathbf{k} \cdot \mathbf{v}_d)^2$ . As  
 189 a first example, we suppose the electron flow is along the  $+x$ -axis, with drift velocity  $v_d = -c_0/10$   
 190 (where  $c_0$  is the speed of light in vacuum). We must emphasize that this value of the drift  
 191 velocity is unrealistically high and is considered here just for illustrative purposes to describe the  
 192 qualitative behavior of surface waves in this nonreciprocal platform. Later in the article, and in  
 193 the Supplemental Material, we provide results for much smaller values of drift velocity. The  
 194 modified SPP dispersion surface is shown in Fig. 1(c). The dispersion asymptote is now tilted  
 195 as a result of the Doppler shift, as discussed in [47], making the dispersion surface strongly  
 196 asymmetric and nonreciprocal in the  $x$ -direction, with a frequency range where SPPs can only  
 197 propagate toward the negative  $x$ -axis. In addition, unidirectional SPPs are now supported at  
 198 frequencies where SPPs could not propagate at all in the reciprocal case (frequencies higher than  
 199 the flat asymptote in Fig. 1(b)). The field distribution of surface waves launched by a vertical  
 200 dipole source is shown in Fig. 1(e) for a frequency higher than the original surface-plasmon  
 201 resonance,  $\omega = 0.8\omega_p > \omega_{SPP}$ . We clearly see that, in this case, SPPs propagate preferentially  
 202 toward left, parallel to the electrons drift velocity, despite the homogeneity and isotropy of the  
 203 surface. While this behavior is somewhat expected as an extension of the 1D results of Ref. [47]  
 204 to a 2D surface, even more extreme wave-propagation effects emerge at different frequencies and  
 205 angles, as discussed in the next sections.

## 206 2.1. Inflexion Points and Slow-Light Beaming

207 The results in Fig. 1 clearly show that the dispersion properties of drift-biased SPPs strongly  
 208 depend on the angle  $\Psi$  between in-plane wavevector and current flow, as expected from the  
 209 spatially dispersive form of the permittivity. To clarify this point further, Figure 2(a) shows

210 1D dispersion curves for SPPs propagating along different angles. SPPs propagating normal  
 211 to the current flow ( $\Psi = 90$  deg.) do not interact with the drifting electrons and the dispersion  
 212 curve is the same as in the reciprocal case with flat asymptotes at  $\omega = \omega_{SPP}$ . Conversely,  
 213 SPPs propagating along the current flow ( $\Psi = 0$ ) are maximally affected by the presence of the  
 214 current, particularly in the large-wavevector asymptotic region where spatial dispersion becomes  
 215 particularly strong. The tilted dispersion asymptote is associated with highly localized SPPs  
 216 dragged by the flow of electrons [47], and its slope (group velocity) is indeed exactly equal to the  
 217 electron drift velocity seen by the SPP mode, i.e.,  $\partial\omega/\partial k = v_d \cdot \hat{u}_k$ , where  $\hat{u}_k$  is the in-plane unit  
 218 wavevector. Such a tilted asymptote makes the dispersion curve non-monotonic for wavevectors  
 219 opposite to  $v_d$ , with an *inflexion point* (red dot in Figure 2(a)) where the SPP group velocity  
 220 vanishes and changes sign. The position of the inflexion point along the frequency axis depends  
 221 on the direction of propagation, such that, for each angle  $\Psi$ , an inflexion point exists at a different  
 222 frequency,

$$\begin{aligned} \omega_{inf} &= \frac{\omega_p}{\sqrt{2}} \left[ 1 - \frac{3v_d \cos(\Psi)}{2c} \left( \frac{c}{2v_d \cos(\Psi)} \right)^{1/3} \right] \\ &\Rightarrow \begin{cases} \omega_{inf}^{min} = \frac{\omega_p}{\sqrt{2}} \left[ 1 - \frac{3v_d}{2c} \left( \frac{c}{2v_d} \right)^{1/3} \right], & \Psi = 0 \\ \omega_{inf}^{max} \rightarrow \frac{\omega_p}{\sqrt{2}}, & \Psi \rightarrow 90 \text{ deg.} \end{cases} \end{aligned} \quad (2)$$

223 Thus, while an inflexion point exists for any angle  $\Psi \in [0, 90)$  deg., its frequency is limited within  
 224 the range  $\omega_{inf}^{min} \leq \omega_{inf} \leq \omega_{inf}^{max}$ , as shown in Fig. 2(b). Minimum inflexion-point frequency  
 225 occurs for SPP propagation along the current flow and maximum frequency is asymptotically  
 226 reached for propagation normal to the current, in which case the inflexion point rapidly migrates  
 227 to large values of wavevector as seen in Fig. 2(a). For any frequency outside this window, no  
 228 inflexion point appears, i.e., the SPP group velocity does not vanish along any direction.

229 The existence of an angle-dependent inflexion point in this frequency window leads to nontrivial  
 230 propagation effects on the 2D surface of the considered nonreciprocal platform. These effects,  
 231 which have not been studied previously, can be elucidated by considering the system's Green  
 232 function under quasi-static approximation. Indeed, while the 3D Green function described above  
 233 provides a complete formulation to study SPP propagation, it is usually evaluated numerically  
 234 and tends to hide physical insight. A simpler, more revealing, approximate formulation can be  
 235 obtained by neglecting retardation effects (quasi-static approximation) and assuming that the  
 236 main radiation channel of the dipolar source is represented by the excitation of a single, guided,  
 237 surface mode. As was shown in Ref. [62], under these approximations, the source radiation  
 238 intensity in a certain in-plane direction (radiated power per unit angle) is given by

$$U(\Psi) \approx \frac{\omega^2}{16\pi} \frac{1}{|\nabla_{\mathbf{k}_t} \omega(\mathbf{k}_t)|} \frac{1}{C(\mathbf{k}_t)} |\boldsymbol{\gamma}^* \cdot \mathbf{E}_{\mathbf{k}}(z_0)|^2, \quad (3)$$

239 where  $\mathbf{k}_t$  is the in-plane wavevector,  $\tan(\Psi) = k_y/k_x$ ,  $\mathbf{E}_{\mathbf{k}}(z_0)$  is the modal electric field at  
 240 the location  $z_0$  of a source with polarization state  $\boldsymbol{\gamma}$ ,  $\omega(\mathbf{k}_t)$  is the dispersion relation of the  
 241 relevant mode (hence,  $\nabla_{\mathbf{k}_t} \omega(\mathbf{k}_t)$  is the group velocity), and  $C(\mathbf{k}_t)$  is the local curvature of the  
 242 equifrequency contour (EFC) of the dispersion relation. Equation (3) gives the approximate  
 243 in-plane radiation pattern of the dipole source, corresponding to the in-plane pattern of SPP  
 244 propagation. This equation reveals that the SPP pattern can be controlled in two ways: (i)  
 245 by suitably selecting the polarization of the dipole source, which controls the coupling factor  
 246  $|\boldsymbol{\gamma}^* \cdot \mathbf{E}_{\mathbf{k}}(z_0)|^2$  between the source and the surface mode of interest; or (ii) by engineering the  
 247 dispersion relation of the relevant surface mode, namely, by controlling the local curvature  $C(\mathbf{k}_t)$   
 248 of the equifrequency contour and/or the wavevector dependence (angular dependence) of the

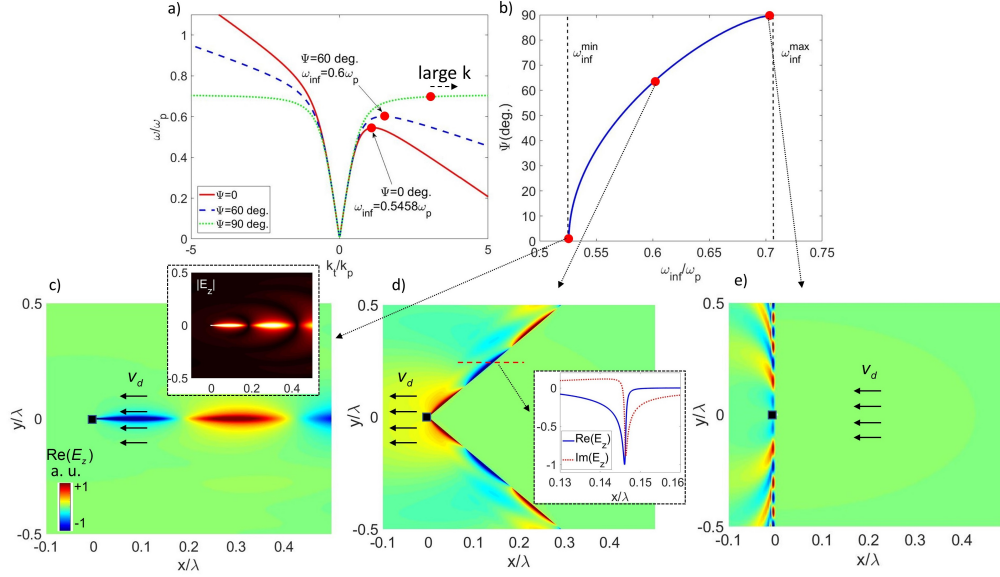


Fig. 2. (a) Dispersion curves for SPPs propagating along different angles with respect to the current flow. The angle  $\Psi$  is measured from the positive  $x$ -axis (see Fig. 1(a)). Different curves correspond to the intersection of the dispersion surface in Fig. 1(c) with planes at angle  $\Psi$  with respect to the  $k_x$ -axis. The red dots indicate inflexion points for different directions of propagation. (b) Inflexion-point frequencies for SPPs propagating along different angles. (c,d,e) Source-excited in-plane distribution of the SPP electric field (time snapshot of the  $z$  component) for (c)  $\omega = \omega_{inf}^{min}$ , (d)  $\omega = 0.6\omega_p$  and (e)  $\omega \approx \omega_{SPP} = \omega_{inf}^{max}$ . The  $x$  and  $y$  axes are normalized with respect to the free-space wavelength at the radiation frequency. The black squares indicate the in-plane position of the source, which is located in the vacuum region at  $z_0 = \lambda/10$  above the interface for panels (c,d) and at  $z_0 = \lambda/30$  for panel (e) (the source is closer to the interface in this panel to efficiently excite the high-wavevector components of the SPPs). The inset in panel (c) shows the amplitude distribution of the  $z$ -component of the electric field, and the inset in panel (d) shows the real and imaginary parts of  $E_z$  along the red dashed line crossing the narrow beam in the main panel.

249 group velocity,  $|\nabla_{\mathbf{k}_t} \omega(\mathbf{k}_t)|$ . In the considered current-biased plasmonic platform, the presence  
 250 of inflexion points where the group velocity vanishes is therefore a crucial factor affecting the  
 251 in-plane propagation pattern. Indeed, at any frequency where an inflexion point appears, the  
 252 inverse of the group velocity in Eq. (3) diverges,  $1/|\nabla_{\mathbf{k}_t} \omega(\mathbf{k}_t)| \rightarrow \infty$  (in practice it becomes large  
 253 but finite) along a specific angle with respect to the current flow. Thus, the in-plane propagation  
 254 pattern is maximized and localized around this angle, resulting in a peculiar “beaming effect” as  
 255 further discussed below.

256 Figure 2(c,d,e) show the in-plane field distributions, calculated using our Green function  
 257 formulation, for SPP propagation at three frequencies: (c) minimum and (e) maximum inflexion-  
 258 point frequencies and (d) another frequency in between. As shown in Fig. 2(a,b), minimum  
 259 inflexion-point frequency corresponds to vanishing SPP group velocity in the direction of the  
 260 current flow. This leads to a diverging behavior in Eq. (3) at  $\Psi = 0$ , which implies that the  
 261 SPP fields form a unidirectional narrow beam along the current flow, as confirmed by Fig.  
 262 2(c). Note that no energy actually propagates toward the  $+x$ -axis since the group velocity is  
 263 zero, and the narrow beam resembles a standing wave with localized and enhanced fields, as  
 264 seen in the field amplitude distribution plotted in the inset of Fig. 2(c) (an animation of the

265 calculated time-harmonic electric field, which further clarifies this peculiar behavior, is included  
 266 as Supplemental Material). Choosing a different frequency, for example  $\omega = 0.6\omega_p$ , an inflexion  
 267 point appears for SPPs propagating at an angle  $\Psi = 60$  deg. with respect to the current flow (see  
 268 Fig. 2(a), dashed blue line). This leads to narrow SPP beams along  $\Psi = \pm 60$  deg., as shown in  
 269 Fig. 2(d). In this scenario, two beams emerge because the system's response is reciprocal normal  
 270 to the current, therefore SPPs propagate symmetrically along the  $y$ -axis. As in the previous case,  
 271 these beams are narrow standing waves with enhanced and localized fields. Interestingly, in  
 272 this case the field distribution is even sharper around  $\Psi = \pm 60$  deg., especially toward smaller  
 273 angles, where no surface-wave propagating solution exists at this frequency (see Fig. 1(c) and  
 274 the equifrequency-contour animation in Supplemental Material). We note that, although the field  
 275 pattern looks discontinuous around this angle, a closer inspection reveals that, rather than an  
 276 actual field discontinuity (which would be nonphysical on a homogeneous surface), the fields  
 277 decay very sharply, within a small fraction of a wavelength, as demonstrated in the inset of  
 278 Fig. 2(d) which shows the real and imaginary parts of the electric field along the red dashed  
 279 line. We speculate that such ultra-sharp fields on a homogeneous surface may be useful for  
 280 surface-sensing applications or optical trapping near the surface. Finally, Fig. 2(e) shows the  
 281 fields at  $\omega \approx \omega_{SPP} = \omega_{inf}^{max}$ , at which an inflexion point appears for SPPs propagating close to  
 282  $\Psi = \pm 90$  deg. Indeed, in this case, the field distribution is dominated by the presence of narrow  
 283 beams almost normal to the current flow and with large wavenumber, consistent with Fig. 2(a).  
 284 The emergence of these narrow, current/frequency-steerable, frozen-light beams with enhanced  
 285 fields is highly nontrivial, especially given the fact that the plasmonic platform that supports  
 286 them is homogeneous, and they may offer new opportunities for tunable, directional, enhanced,  
 287 light-matter interactions on plasmonic surfaces.

## 288 2.2. Unidirectional Propagation and Negative Group Velocity

289 As discussed above, for frequencies higher than  $\omega_{inf}^{max} = \omega_{SPP}$  or lower than  $\omega_{inf}^{min}$ , no inflexion  
 290 point appears, and hence the SPP group velocity never vanishes along any in-plane direction.  
 291 In these frequency regions, it is mostly the curvature of the equifrequency contour  $C(\mathbf{k}_t)$  that  
 292 determines, according to Eq. (3), how SPPs propagate on the two-dimensional interface. Other  
 293 anomalous wave-propagation effects occur in this regime, qualitatively different from the behavior  
 294 of SPPs in the  $\omega_{inf}^{min} < \omega < \omega_{inf}^{max}$  window. Figure 3(a) shows the dispersion surface with  
 295 two cut-planes at constant frequencies,  $\omega = 0.8\omega_p > \omega_{SPP}$  and  $\omega = 0.52\omega_p < \omega_{inf}^{min}$ . The  
 296 intersection of these planes with the dispersion surface gives the EFCs presented in Fig. 3(b) and  
 297 3(c), respectively (an animation of how the EFC changes as a function of frequency is included  
 298 as Supplemental Material). The colors of the density plots correspond to the magnitude of the  
 299 integrand in Eq. (33) of the Supplemental Material (brighter colors mean higher intensity),  
 300 indicating which portions of the EFC contribute more strongly to SPP excitation for the chosen  
 301 source, i.e., a dipolar emitter linearly-polarized along the  $z$ -axis and located above the interface  
 302 as detailed in the caption of Fig. 1. The white arrows, normal to the EFC at each point, indicate  
 303 the main directions of energy flow (group velocity vectors). As Fig. 3(b) suggests, at  $\omega = 0.8\omega_p$   
 304 SPPs are expected to propagate unidirectionally toward the  $-x$ -axis (propagation along the  $+x$ -axis  
 305 is prohibited) with wavefront spreading (diffraction) along the  $y$ -axis. The field distribution in  
 306 Figure 1(e) confirms this behavior. Further comments on this propagation pattern and on the  
 307 impact of the source height from the surface are discussed in the Supplemental Material.

308 The equifrequency contour has a more complicated non-connected shape for frequencies  
 309 lower than  $\omega_{inf}^{min}$  due to the tilted dispersion asymptote. As seen in Fig. 3(c), the contour is  
 310 formed by a central ellipse slightly stretched toward right (in the absence of current bias, the  
 311 central ellipse becomes a circle) and an approximately vertical line at larger positive values  
 312 of  $k_x$ . This vertical line corresponds to the large-wavevector SPPs dragged backward by the  
 313 drifting electrons, propagating with group velocity almost exactly equal to the drift velocity,

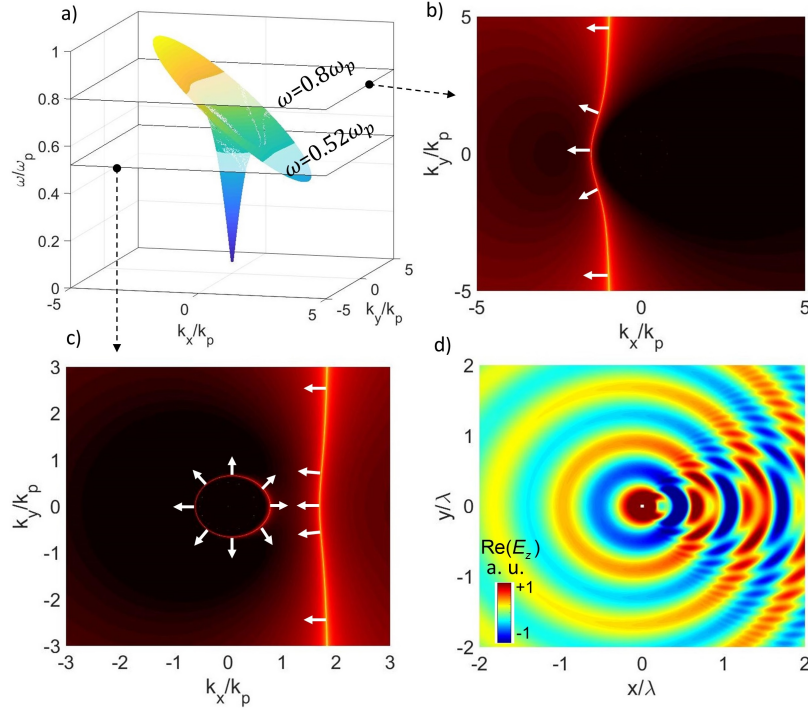


Fig. 3. (a) SPP dispersion surface for  $v_d = -c/10$  with two cut-planes at constant frequency,  $\omega = 0.8\omega_p$  and  $\omega = 0.52\omega_p$ . The cross sections correspond to the equipfrequency contours (EFC) shown in panels (b) and (c). EFCs are represented as density plots of the magnitude of the integrand of the 3D Green function in Eq. (33) of the Supplemental Material. The source-excited electric field distribution (time snapshot of the  $z$  component) at  $\omega = 0.8\omega_p$ , corresponding to panel (b), is shown in Fig. 1(e), whereas panel (d) shows the field distribution at  $\omega = 0.52\omega_p$ , corresponding to the EFC in panel (c).

314 as discussed in the previous sections. If the drift velocity is reduced, the vertical line moves  
 315 to even larger values of  $k_x$ , going asymptotically to infinity for  $v_d \rightarrow 0$ . As the direction of  
 316 the white arrows in Fig. 3(c) suggests, small-wavevector SPPs are allowed to propagate along  
 317 every in-plane direction with a slight preference toward the  $+x$ -axis (ellipse contribution), but  
 318 the dipole radiation may also couple to counter-propagating SPPs with positive  $k_x$  but negative  
 319 group velocity (vertical line contribution). Figure 3(d) shows the corresponding source-excited  
 320 field distribution at  $\omega = 0.52\omega_p$ , demonstrating an asymmetric SPP wavefront, stronger toward  
 321 the positive  $x$ -axis, and characterized by a clear interference pattern due to the two contributions  
 322 in Fig. 3(c). An animation of the calculated time-harmonic electric field, corresponding to Fig.  
 323 3(d), is included as Supplemental Material. At lower frequencies, the EFC and field distribution  
 324 are qualitatively similar to those in Fig. 3(c,d), but SPP propagation tends to become more  
 325 symmetric and isotropic as frequency is lowered, consistent with the fact that the elliptical EFC  
 326 becomes smaller and rounder (smaller wavevectors imply weaker spatial dispersion), whereas the  
 327 vertical-line contribution tails off as it moves to larger values of  $k_x$  (hence, such large-wavevector  
 328 SPPs become increasingly difficult to excite).

329 We also note that, while the results in this section and the previous section have assumed  
 330 an unrealistically high value of drift velocity for illustrative purposes, the nonreciprocal effects

331 demonstrated here can be achieved at much lower drift velocities (examples are provided in  
 332 Section 3 and in the Supplemental Material). In principle, as long as the drift velocity is nonzero,  
 333 the plasmonic material remains nonreciprocal, but the nonreciprocal behavior may become so  
 334 weak as to be overshadowed by dissipative and other effects. The non-trivial impact of dissipation  
 335 on the modal dispersion is discussed in the next section. Furthermore, other forms of nonlocality,  
 336 e.g., of hydrodynamic origin, may have an impact if dissipation is sufficiently weak. While a  
 337 complete analysis of these nonlocal effects will be the subject of a future work, we expect that  
 338 similar tradeoffs may exist as in nonreciprocal magnetic-biased plasmonic systems [1, 8, 11, 69].

### 339 2.3. Modal Transitions, Exceptional Points, and Impact of Dissipation

340 Since the inflexion point described above represents the most important feature of the dispersion  
 341 diagram of a current-biased plasmonic system, marking the transition between different wave-  
 342 propagation regimes, we further investigated the local dispersion behavior around this point and  
 343 the impact of dissipation. Let us consider SPPs with propagation direction fixed parallel to the  
 344 drift current,  $\Psi = 0$ , i.e., with their in-plane wavevector purely in the  $x$ -direction. The dispersion  
 345 diagram for this case is plotted again in Fig. 4(a), but tracking each individual solution of the  
 346 dispersion equation, including where the longitudinal modal wavenumber becomes complex, as  
 347 frequency is varied, and assuming this is a 1D propagation scenario where  $k_y$  is forced to be  
 348 zero. Mathematically, solutions of the dispersion equation cannot simply disappear as frequency  
 349 (assumed real) is varied; therefore, above the inflexion point, solutions still exist but they are  
 350 expected to correspond to evanescent modes. In other words, the inflexion point acts as a cut-off  
 351 frequency or band edge and, as seen in Fig. 4(a), the local dispersion around this point resembles  
 352 the typical *square-root-like bifurcation* around an exceptional point of degeneracy (EP) [66, 67].

353 To clarify this behavior, Fig. 4(b,c,d) show the modal solutions (SPP poles) on the complex  
 354  $k_x$ -wavenumber plane as frequency is increased. At frequencies lower than the inflexion point,  
 355 i.e.,  $\omega < \omega_{inf}$ , owing to the downward bending of the dispersion curve we have two counter-  
 356 propagating modes (opposite group velocity) on the positive side of the real  $k_x$  axis (Fig. 4(b)).  
 357 Right at the inflexion point, these two modes/poles coalesce into a single mode with vanishing  
 358 group velocity (Fig. 4(c)). Finally, for frequencies higher than the inflexion-point,  $\omega > \omega_{inf}$ ,  
 359 the poles rapidly migrate away from the real axis (Fig. 4(d)), leading to an interesting modal  
 360 transition further discussed below. This behavior indeed suggests that the inflexion point could  
 361 also be interpreted, in this 1D propagation scenario, as an exceptional point of degeneracy since  
 362 it marks the coalescence and branching of modes [66, 67].

363 To further confirm this interpretation, we considered the general conditions that a solution of  
 364 the dispersion equation, in a 1D wave-guiding system, must satisfy to be identified as an EP, as  
 365 originally derived in [63–65]. The first necessary condition to obtain a first-order EP is that two  
 366 first-order roots of the dispersion equation,  $D(k_{EP}, \omega_{EP}) = 0$ , coalesce to form a second-order  
 367 root, which implies that, at the EP,

$$D(k_{EP}, \omega_{EP}) = \left. \frac{\partial D(k, \omega)}{\partial k} \right|_{\substack{k=k_{EP} \\ \omega=\omega_{EP}}} = 0 \quad (4)$$

368 where  $k_{EP}$  and  $\omega_{EP}$  are the wavenumber and angular frequency at which the degeneracy emerges.  
 369 However, an EP should also satisfy an additional condition,

$$\left. \frac{\partial D(k, \omega)}{\partial \omega} \cdot \frac{\partial^2 D(k, \omega)}{\partial k^2} \right|_{\substack{k=k_{EP} \\ \omega=\omega_{EP}}} \neq 0. \quad (5)$$

370 In fact, only if Eq. (5) is satisfied, then the second-order root becomes a branch point (and not  
 371 a saddle point) where various branches of the dispersion function  $k(\omega)$  merge [63–65]. Our  
 372 numerical tests applied to the case of SPPs propagating along the electron current verify that

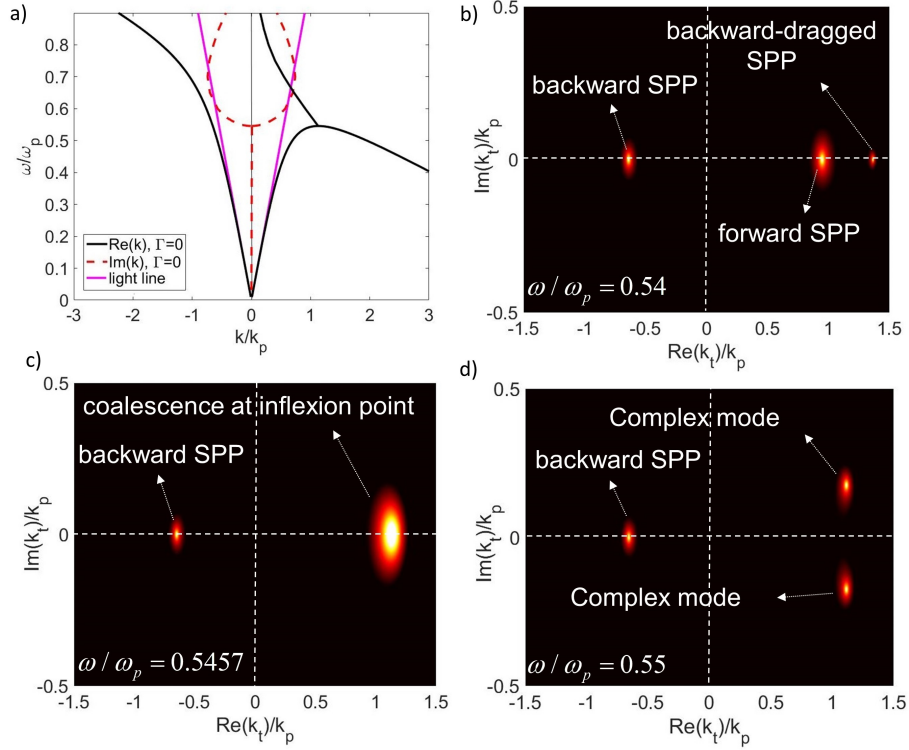


Fig. 4. (a) Dispersion diagram for SPPs propagating in the direction of the current flow ( $\Psi = 0$ ), similar to Fig. 2(a), but tracking each individual solution of the dispersion equation, and plotting its complex in-plane modal wavenumber, as frequency is varied. Absorption losses are assumed to be zero, i.e.,  $\Gamma = 0$ . See Fig. 5 for the dissipative case. Solid purple lines indicate the light cone. (b,c,d) SPP pole constellation, on the complex  $k_x$ -plane (for fixed  $k_y = 0$ ), at different frequencies: (a)  $\omega/\omega_p = 0.54 < \omega_{inf}^{min}$ , (b)  $\omega/\omega_p = 0.5457 = \omega_{inf}^{min}$  and (c)  $\omega/\omega_p = 0.55 > \omega_{inf}^{min}$ , for SPP modes propagating along the drifting electrons with  $v_d = -c/10$ . The peculiar character of the two complex modes in panel (d) is discussed in the text.

373 the local 1D dispersion function,  $k_x(\omega)$  (for  $k_y = 0$ ), satisfies conditions (4) and (5) around  
 374 the inflexion frequency (red point in Fig. 2(a)), hence confirming that in this 1D scenario,  
 375 the inflexion point can be interpreted as an EP (branch point) where forward-propagating and  
 376 backward-dragged SPPs coalesce. We also note that, unlike typical EPs in open non-Hermitian  
 377 systems, the EP observed here exists in a system with no balanced distribution of loss and gain.  
 378 Indeed, this dispersion feature is more similar to the EPs associated with the band edges of  
 379 lossless periodic structures (see, for example, Refs. [61, 67, 68]); however, in the considered  
 380 current-biased system, the EP exists at a sort of unidirectional band edge (the inflexion point)  
 381 created not by a periodic modulation, but by the Doppler shift resulting from the applied current.  
 382 The modal transition occurring through this EP is particularly interesting as it leads to a  
 383 rich and subtle behavior at higher frequencies, and some additional observations should be  
 384 made. As discussed in Ref. [1], in a system with continuous translational symmetry as the one  
 385 considered here, a *direct* transition from a purely propagating solution to a purely evanescent one,  
 386 or viceversa, can only occur at band edges or cut-off frequencies at zero or infinite wavenumbers  
 387 (where the modal wavenumber can go *directly* from purely real to purely imaginary). This is

388 clearly not the case in Fig. 4(a), where the band edge (exceptional point) exists in the dispersion  
389 diagram at a finite non-zero value of wavenumber and the solutions above the EP frequency  
390 are indeed complex, with the same real part but opposite imaginary parts. However, since we  
391 assumed that the considered structure is lossless,  $\Gamma = 0$ , a complex wavenumber is puzzling  
392 because it implies some form of energy dissipation or gain as the wave propagates (the solution  
393 is not purely evanescent, as it is instead in a lossless photonic bandgap, or below cut-off in a  
394 lossless closed waveguide). One of the two complex solution branches above the EP in Fig. 4(a)  
395 is clearly non-physical because it represents a growing propagating wave whereas the system  
396 is passive. We should note here that a direct current bias may in principle lead to optical gain  
397 through negative Landau damping even in an otherwise passive system: if the drift velocity is  
398 comparable and greater than the wave phase velocity,  $v_d > \omega/k$ , the electrons “trapped” inside  
399 the moving potential wells of the wave lose kinetic energy to the wave (the opposite process is the  
400 regular Landau damping discussed in the following) [52, 60]. However, this cannot happen in the  
401 present situation since the SPP phase velocity in the region of interest of the dispersion diagram  
402 is much larger than  $v_d$ . In addition, it was argued in [52] that SPP amplification and instability are  
403 not possible in a configuration with a single drift-biased plasmonic medium. Going back to our  
404 discussion of the dispersion diagram in Fig. 4(a), we note that the other solution branch above  
405 the EP corresponds, instead, to a physical, decaying, propagating wave that becomes overdamped  
406 as it crosses the light line at higher frequencies, which suggests that radiation leakage plays  
407 an important role in this behavior. In fact, analogous modal transitions (albeit for reciprocal  
408 systems) were observed and investigated in the context of leaky-wave antennas a few decades  
409 ago [70, 71]. In the transition region between bound- and leaky-waves, it was similarly observed  
410 that certain solutions are non-physical (growing), and the unexpectedly lossy solutions below  
411 the light line, in an otherwise lossless structure, can be explained as the “winding down” of the  
412 leaky-wave solution right under the light cone (with a virtually negligible contribution to the  
413 total fields excited by an actual source [71]).

414 Finally, we investigated how the dispersion diagram changes when absorption losses are  
415 included in the current-biased plasmonic material. This is particularly important considering the  
416 virtually unavoidable presence of dissipation mechanisms in plasmonic media. In particular, here  
417 we first studied the impact of the intrinsic (bulk) scattering losses of the material, modeled by an  
418 intrinsic damping rate  $\Gamma$  which is assumed to be unaltered by the presence of the current bias, as  
419 done for example in [52]. However, how this damping rate affects the propagation and attenuation  
420 of SPPs strongly depends on the presence and velocity of the drift current, the SPP wavevector,  
421 and the specific structure. As seen in Fig. 5(a,b), increasing  $\Gamma$  determines an increase in the  
422 imaginary part of the modal wavenumber, especially in the large-wavevector regime, as expected.  
423 Non-zero dissipation also “opens” the band bifurcation at the EP, such that the dispersion curves  
424 no longer flatten out completely. This behavior is therefore qualitatively different from the way  
425 losses affect nonreciprocal SPPs in magnetically biased plasmas [1, 8], where band edges are  
426 located at diverging values of wavenumber. As a result of this modified dispersion diagram, the  
427 effects described in Section 2.1, which mostly depend on a slowing down of the group velocity  
428 at the inflexion point, are expected to be sensitive to the presence of dissipation (which may  
429 actually be useful for the sensing of absorbing layers on the plasmonic platform). Figure 5(b,c)  
430 compare two cases where  $\Gamma$  is kept fixed but the drift velocity is decreased. As seen here, by  
431 reducing the drift velocity, the imaginary part of the modal wavenumber generally increases,  
432 indicating that, in this configuration, drift-induced nonlocality and nonreciprocity may indirectly  
433 mitigate the detrimental impact of scattering losses by modifying the dispersion diagram and  
434 the group velocity of the modes. Finally, if losses are sufficiently large and the drift velocity is  
435 low (Fig. 5(d)), dissipation starts to dominate over the drift-induced nonlocal and nonreciprocal  
436 effects. In particular, the backward-propagating mode now exhibits the typical “back-bending” of  
437 a lossy SPP (real dispersion curve bends in the opposite direction) and becomes overdamped

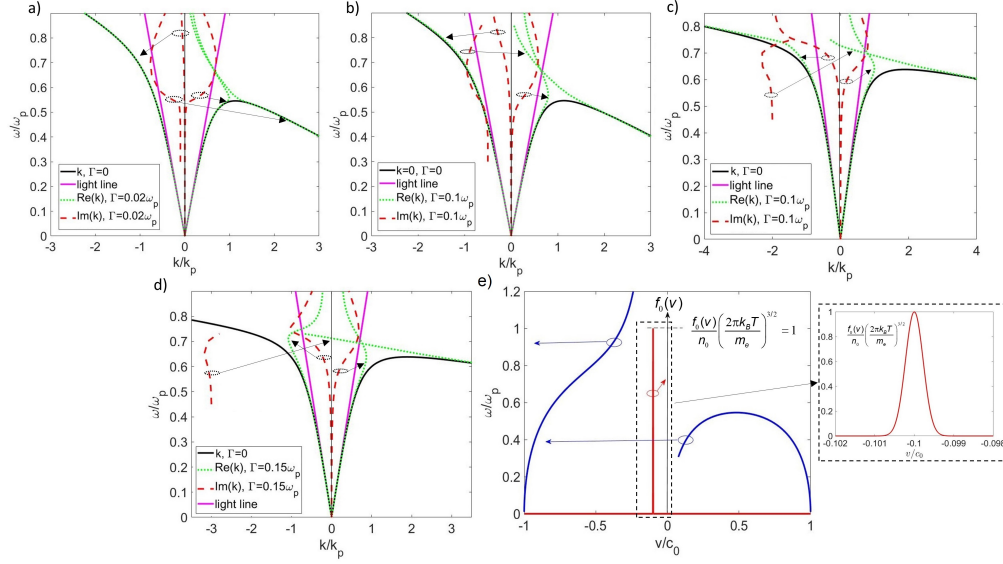


Fig. 5. Impact of dissipation on nonreciprocal current-biased SPPs. (a,b) Dispersion curves for SPPs propagating along the current flow, with  $v_d = -c/10$  in the presence of intrinsic (bulk) scattering losses: (a)  $\Gamma = 0.02\omega_p$  and (b)  $\Gamma = 0.1\omega_p$ . (c,d) Dispersion curves for SPPs propagating along the current flow, with  $v_d = -c/40$  and (c)  $\Gamma = 0.1\omega_p$  and (d)  $\Gamma = 0.15\omega_p$ . For the forward-propagating mode with largest wavevector, the imaginary part is plotted over a limited frequency range due to numerical difficulties in tracking this solution beyond this range. Solid black lines denote the lossless case (showing only the real branches for simplicity), and dotted green and dashed red lines indicate the real and imaginary part of the in-plane modal wavenumber,  $\text{Re}(k)$  and  $\text{Im}(k)$ , respectively. Arrows indicate which imaginary and real branches correspond to the same mode. Solid purple lines denote the light cone. (d) Phase velocity of SPP modes propagating parallel to the drifting electrons with  $v_d = -c/10$ , compared with a Maxwell-Boltzmann velocity distribution for a typical plasmonic material at room temperature and with the same electron drift velocity. The inset shows a zoomed-in view of the distribution function.

438 at higher frequencies ( $\text{Re}[k] < \text{Im}[k]$ ), whereas it was still underdamped in Fig. 5(c).  
 439 The smaller-wavevector branch of the forward-propagating mode shows a similar back-bending  
 440 behavior (as it does in all cases in Fig. 5), whereas the other, flatter branch becomes overdamped  
 441 over a broad range of wavevectors (and for larger wavevectors it is essentially a dark mode,  
 442 increasingly difficult to excite). Unidirectional propagation is no longer possible in this regime  
 443 as the forward- and backward-propagating modes are both allowed to propagate at low frequencies  
 444 and, as frequency increases, they become overdamped almost simultaneously.

445 In addition to intrinsic scattering loss, another potentially important attenuation mechanism  
 446 in drift-biased plasmas and plasmonic materials is bulk Landau damping, which exists even  
 447 in the absence of any collisions, originating instead from the kinetic energy transfer from an  
 448 electromagnetic wave to the electrons “trapped” inside its moving potential wells. This effect  
 449 is possible if the velocity distribution function is not a delta function centered at the drift-bias  
 450 velocity (cold biased plasma), but follows for example a Maxwell-Boltzmann distribution  $f_0(v)$   
 451 for a plasma at non-zero temperature. The attenuation due to bulk Landau damping can be shown  
 452 to be proportional to the velocity derivative  $\partial_v f_0(v)$  [55, 60], which indicates that this form of  
 453 damping is important if the electron velocities are close to, and smaller, than the wave phase

454 velocity. For the considered drift-biased nonreciprocal configuration, Figure 5(d) compares the  
 455 phase velocity of SPPs propagating along the current with the Maxwell-Boltzman distribution  
 456 function for a typical plasmonic material at 300K. With the exception of the backward-propagating  
 457 mode at very large frequencies, the phase velocity of the SPP modes lies far out on the distribution  
 458 tail, where  $\partial_v f_0(v) \simeq 0$ , which implies that the presence of bulk Landau damping can be  
 459 safely ignored in the present case. We also note that another form of Landau damping, namely,  
 460 surface-collision-induced damping, associated with the direct excitation of electron-hole pairs  
 461 by the highly confined electric field on the interface [11], may be more significant in this case,  
 462 but is still expected to be smaller than the intrinsic (bulk) scattering losses of typical solid-state  
 463 plasmonic media.

464 The analysis presented in this section shows, for the first time to the best of our knowledge, the  
 465 impact of dissipation (due to collisions or Landau damping) on the drift-induced nonlocal and  
 466 nonreciprocal effects in current-biased 3D plasmonic platforms. While the presence of losses is  
 467 detrimental for wave-guiding applications, the next section discuss an example of application of  
 468 nonreciprocal drift-biased plasmonics where losses are actually necessary, namely, near-field  
 469 radiative heat transfer mediated by SPPs.

### 470 3. Current-Induced Nonreciprocal Radiative Heat Transfer

471 We consider the canonical problem of near-field radiative heat-transfer between two planar bodies,  
 472 as shown in Fig. 6(a): two plasmonic slabs, with permittivity  $\epsilon(\omega) = 1 - \omega_p^2(1 + i\Gamma/\omega)/(\omega + i\Gamma)^2$ ,  
 473 are separated by a distance  $d_g$ , and backed by perfect electric conductors. DC electric currents  
 474 are driven in each conductor separately to break reciprocity. As discussed in the previous section,  
 475 the current-biased plasmonic materials can then be approximately described by a spatially and  
 476 frequency dispersive Doppler-shifted permittivity function  $\epsilon(\omega) \rightarrow \epsilon(\omega - \mathbf{k} \cdot \mathbf{v}_d)$ . The considered  
 477 geometry and the following calculations parallel the ones in Ref. [38], but with the crucial  
 478 difference that here we consider, for the first time, a direct current bias to realize nonreciprocal  
 479 radiative heat transfer, instead of magnetized magneto-optical materials.

480 From the fluctuation dissipation theorem [72], the strength of the fluctuating current sources  
 481 that generate thermal radiation is proportional to the imaginary part of the permittivity,  $\text{Im}(\epsilon) \equiv$   
 482  $(\epsilon - \epsilon^*)/2i$ . Unlike many photonic applications in which reducing material absorption is an  
 483 important goal, thermal photonic applications do require materials with non-zero losses since,  
 484 due to thermodynamics constraints, a lossless structure does not generate any thermal emission.  
 485 This relation between absorption and emission is however a subtle one, as discussed in the  
 486 following. In the setup in Fig. 6(a), we are interested in the radiative heat flux density from body  $i$   
 487 to body  $j$ ,  $S_{ij}$ , and vice versa, which is defined as the power density absorbed by body  $j$  from the  
 488 radiated electric and magnetic fields generated by the fluctuating currents in body  $i$ . The total heat  
 489 flux density from body 1 to body 2 can be expanded in terms of its time-harmonic plane-wave  
 490 contributions, i.e., a continuous set of “channels” defined by their wavevector,  $\mathbf{k} = \pm(\mathbf{k}_z + \mathbf{k}_t)$ ,  
 491 and frequency,  $\omega$ , [38]

$$S_{12} = \int_0^\infty \frac{d\omega}{2\pi} \int \frac{d\mathbf{k}_t}{(2\pi)^2} \Phi(T_1, \omega) S_{12}(\mathbf{k}_t, \omega) \quad (6)$$

where  $\Phi(T, \omega) = \hbar\omega \left[ \frac{1}{2} + \frac{1}{\exp(\hbar\omega/K_B T) - 1} \right]$  is the mean energy of photons per frequency  $\omega$  at  
 temperature  $T$  and

$$S_{12}(\mathbf{k}_t, \omega) = \text{Tr} \left( \left[ \hat{\mathbf{I}} - \hat{R}_2^\dagger(\mathbf{k}_t, \omega) \hat{R}_2(\mathbf{k}_t, \omega) \right] \hat{D}_{12}(\mathbf{k}_t, \omega) \right. \\ \left. \times \left[ \hat{\mathbf{I}} - \hat{R}_1(\mathbf{k}_t, \omega) \hat{R}_1^\dagger(\mathbf{k}_t, \omega) \right] \hat{D}_{12}^\dagger(\mathbf{k}_t, \omega) \right) \quad (7)$$

for propagating waves,  $|\mathbf{k}_t| < \omega/c$ , and

$$S_{12}(\mathbf{k}_t, \omega) = \text{Tr} \left( \left[ \hat{R}_2^\dagger(\mathbf{k}_t, \omega) - \hat{R}_2(\mathbf{k}_t, \omega) \right] \hat{D}_{12}(\mathbf{k}_t, \omega) \right. \\ \left. \times \left[ \hat{R}_1(\mathbf{k}_t, \omega) - \hat{R}_1^\dagger(\mathbf{k}_t, \omega) \right] \hat{D}_{12}^\dagger(\mathbf{k}_t, \omega) e^{-2\alpha d_g} \right) \quad (8)$$

492 for evanescent waves,  $|\mathbf{k}_t| > \omega/c$ . The heat flux density from body 2 to body 1 can be obtained  
 493 from Eqs. (7) and (8) by exchanging the subscripts 1 and 2 and changing the temperature in  
 494 Eq. (6) from  $T_1$  to  $T_2$ . In the above equations,  $\alpha$  is the decay rate of evanescent waves along  
 495 the  $z$ -axis,  $R_i(\mathbf{k}_t, \omega)$  is the reflectivity matrix of body  $i$ , whose elements are the reflection  
 496 coefficients for light incident from vacuum, for both transverse-electric and transverse-magnetic  
 497 polarizations, and the parameter  $\hat{D}_{12} = \left[ \hat{I} - \hat{R}_2^\dagger(\mathbf{k}_t, \omega) \hat{R}_1(\mathbf{k}_t, \omega) e^{-i2k_z d_g} \right]$  represents multiple  
 498 reflections between the two bodies (see Ref. [38] for more details). This formalism allows us to  
 499 calculate the near-field 3D heat transfer between two planar slabs with and without a current bias.  
 500 As in our 3D Green function formalism in Section 2 and Supplementary Note III, the presence of  
 501 a non-zero drift current modifies the permittivity, making it wavevector-dependent, and therefore  
 502 changes the reflection coefficients for plane-wave incidence.

503 The existence of a nonzero net heat flow in a two-body geometry as in Fig. 6(a) requires a  
 504 temperature gradient, as dictated by the Second Law of Thermodynamics. In other words, if the  
 505 two bodies are at the same temperature, the total heat flux densities between them are identical,  
 506  $S_{12} = S_{21}$  (integrated over frequency and wavevector), independent of whether the system is  
 507 reciprocal or not. It is then possible to show that thermodynamics imposes the same symmetry also  
 508 for the individual contributions, i.e.,  $S_{12}(\mathbf{k}_t, \omega) = S_{21}(\mathbf{k}_t, \omega)$ , again independent of reciprocity or  
 509 the lack thereof. Interestingly, Ref. [38] demonstrated that reciprocity imposes another symmetry  
 510 constraint for opposite in-plane wavevectors:  $S_{12}(\mathbf{k}_t, \omega) = S_{12}(-\mathbf{k}_t, \omega) = S_{21}(-\mathbf{k}_t, \omega)$ . In a  
 511 nonreciprocal system, this symmetry constraint can be violated since the dispersion diagram is  
 512 no longer necessarily symmetric,  $\omega(\mathbf{k}_t) \neq \omega(-\mathbf{k}_t)$ . As a result,  $S_{12}(\mathbf{k}_t, \omega) \neq S_{12}(-\mathbf{k}_t, \omega) =$   
 513  $S_{21}(-\mathbf{k}_t, \omega)$ , which implies that if heat transfer from body 1 to body 2 occurs through a  
 514 certain wavevector-channel,  $\mathbf{k} = \mathbf{k}_z + \mathbf{k}_t$ , the transfer from body 2 to 1 does not have to occur  
 515 symmetrically through the time-reversed channel,  $\mathbf{k}_{\text{TR}} = -\mathbf{k}_z - \mathbf{k}_t = -\mathbf{k}$ , whose contribution  
 516 can even be zero; the reverse transfer can now occur entirely through a different channel with  
 517 the same  $\mathbf{k}_t$ , i.e., the specular one,  $\mathbf{k}_S = -\mathbf{k}_z + \mathbf{k}_t$ . This results in a persistent heat current  
 518 between the two bodies even at thermal equilibrium (bodies at the same temperature) [37, 38].  
 519 In other words, while a nonreciprocal body may emit strongly in a certain direction defined by  
 520  $\mathbf{k}$  (at a certain frequency), it could be designed to absorb very weakly in that same direction  
 521 (i.e., for  $-\mathbf{k}$ ) and frequency, corresponding to a breaking of Kirchhoff's law of thermal radiation  
 522 (equal absorptivity and emissivity at each direction and frequency) [30, 73–75]. We stress again  
 523 that the existence of a persistent heat current at equilibrium or a violation of Kirchhoff's law in  
 524 these systems does not break thermodynamic laws, since the total net heat flow into each body  
 525 is still zero when the bodies have the same temperature. In the following, we provide the first  
 526 theoretical demonstration of these effects in a platform that does not require magneto-optical or  
 527 space-time-modulated media.

528 First we consider the reciprocal scenario with no current bias in either the lower or upper  
 529 body. In this situation the material permittivity takes a local and isotropic form,  $\epsilon(\omega) =$   
 530  $1 - \omega_p^2 (1 + i\Gamma/\omega) / (\omega + i\Gamma)^2$ , where we assume the same plasma frequency,  $\omega_p$ , and scattering  
 531 rate,  $\Gamma = 0.1\omega_p$ , for both materials. Figure 6(b) shows the heat flux density at each frequency and  
 532 in-plane wavenumber. As expected for reciprocal materials, the heat flux density is symmetric  
 533 with respect to in-plane wavenumber,  $S_{12}(\mathbf{k}_t, \omega) = S_{12}(-\mathbf{k}_t, \omega)$ , and the same plot is obtained  
 534 for any in-plane direction  $\Psi$  since the considered material is laterally homogeneous and isotropic.  
 535 We also verified that this wavevector- and frequency-resolved heat transfer map from body 1  
 536 to 2,  $S_{12}(\mathbf{k}_t, \omega)$ , is identical to the corresponding one from body 2 to 1,  $S_{21}(\mathbf{k}_t, \omega)$ , therefore

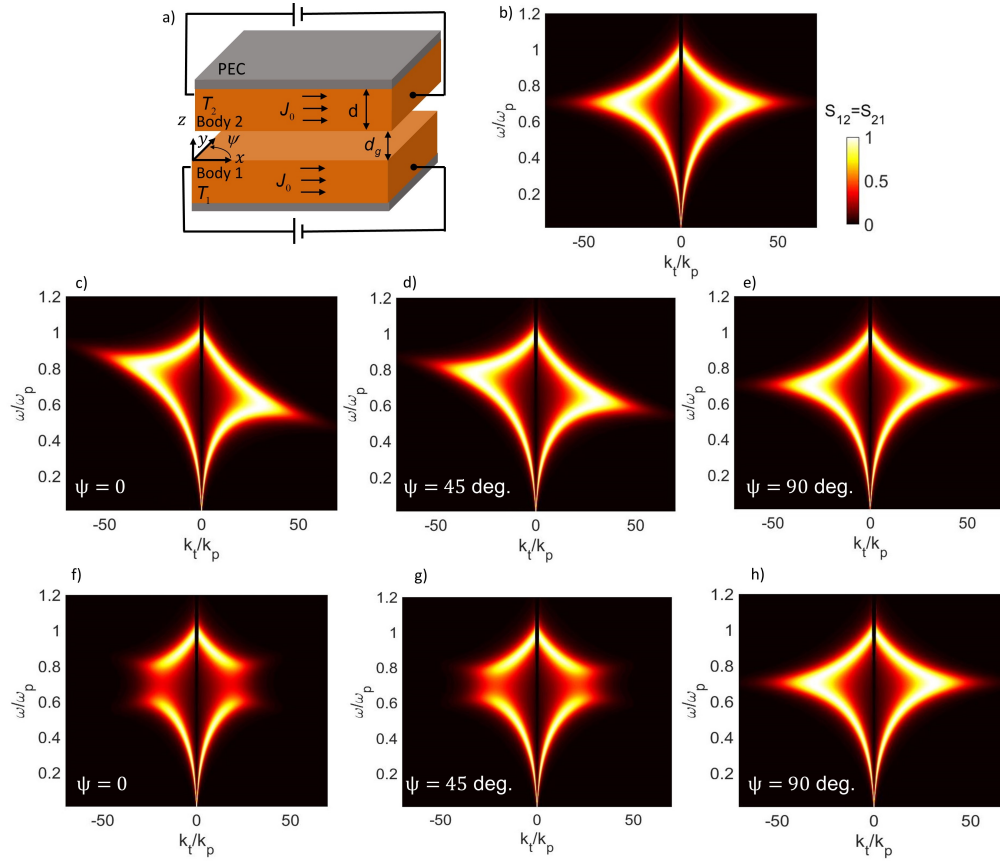


Fig. 6. (a) Geometry considered for investigating the near-field radiative heat transfer between two planar bodies in the reciprocal and nonreciprocal (current-biased) cases. Two planar conducting slabs are placed at a distance  $d_g = \lambda_p/100$  from each other and biased by DC electric currents driven through each conductor separately. The thickness of the slabs is  $d = \lambda_p$ , where  $\lambda_p$  is the free-space wavelength at the plasma frequency. The two slabs are supposed to have identical plasma frequencies and damping rate,  $\Gamma = 0.1\omega_p$ . (b) Heat flux density between the two bodies as a function of frequency and in-plane wavenumber when the current bias is set to zero. Identical heat flux density maps are obtained in this case for any in-plane direction defined by the angle  $\Psi$  with respect to the  $+x$ -axis. (c,d,e) Heat flux density when the two conducting bodies are biased by identical DC currents with  $v_d = -c/300$  along the  $+x$ -axis. The three panels show the heat flux density map for different in-plane directions. (f,g,h) Similar to (c,d,e) but for counter-propagating DC currents in the two conducting bodies.

537 respecting the second law of thermodynamic. We also note that the specific shape of the  
 538 heat flux density in Fig. 6(b) is a result of coupling between the surface waves supported by  
 539 the two interfaces, which strongly modifies their individual dispersion diagram. For deeply  
 540 subwavelength gaps between the two slabs, as in Fig. 6, the structure supports strongly confined  
 541 SPPs, for which even relatively small values of drift velocity determine large changes in their  
 542 response, as seen in our results discussed in the following.

543 We make the system nonreciprocal by biasing the two conductors with an identical direct  
 544 current with  $v_d = -c/300$  (much lower than in previous sections) along the  $+x$ -axis. The heat

545 transfer spectra for this nonreciprocal system are shown in Figs. 6(c,d,e) for different in-plane  
546 wavevector directions, defined by the angle  $\Psi$  with respect to the current flow. As seen from  
547 these results,  $S_{12}(\mathbf{k}_\tau, \omega) \neq S_{12}(-\mathbf{k}_\tau, \omega)$  for any in-plane direction except at  $\Psi = 90$  deg., which  
548 is consistent with our previous observation that there is no interaction between surface waves  
549 and drifting electrons for wavevectors normal to the current flow. In this latter situation, the  
550 heat flux density is exactly the same as in the reciprocal scenario in Fig. 6(b). These results  
551 clearly demonstrate that the such a magnet-free current-biased system exhibits a signature of  
552 nonreciprocity for near-field radiative heat transfer, which implies, as mentioned above, the  
553 presence of a persistent heat current between the two bodies even when they are kept at the same  
554 temperature. Interestingly, the asymmetric heat transfer spectra in Figs. 6(c,d) are qualitatively  
555 different from the ones obtained with magneto-optical materials in [38]. In particular, the  
556 heat transfer spectra in [38] follow the characteristic magnetic-field-induced asymmetry in the  
557 flat dispersion asymptotes of surface magneto-plasmons, whereas our results in Figs. 6(c,d)  
558 show an asymmetry that arise from a Doppler-shift-induced tilt of the dispersion asymptotes.  
559 Furthermore, we have again verified that the current-biased system still respects the constraint  
560  $S_{12}(\mathbf{k}_\tau, \omega) = S_{21}(\mathbf{k}_\tau, \omega)$ , which needs to be satisfied regardless of the local or nonlocal and  
561 reciprocal or nonreciprocal nature of the system.

562 Finally, as in Ref. [38], we show that the breaking of reciprocity for the individual bodies  
563 does not necessarily lead to an asymmetric heat transfer spectrum. We consider a scenario  
564 in which the two plasmonic planar bodies are biased with direct currents with the same drift  
565 velocity but opposite directions,  $v_{d,1} = -v_{d,2} = -c/300$ , along the  $+x$ -axis. In this scenario, each  
566 subsystem individually supports nonreciprocal surface modes but with asymmetric dispersion  
567 (tilted asymptotes) along opposite directions. Since these nonreciprocal SPP modes existing  
568 on the individual interfaces are strongly coupled through the gap, the resulting SPP dispersion  
569 diagram becomes symmetric, and the asymmetry in heat transfer density is also expected to  
570 disappear in this scenario. Indeed, Figs. 6(f,g,h) verify that  $S_{12}(\mathbf{k}_\tau, \omega) = S_{12}(-\mathbf{k}_\tau, \omega)$  for different  
571 in-plane directions, demonstrating that, also in current-biased systems, as in magneto-optical  
572 implementations, the breaking of electromagnetic reciprocity is a necessary but insufficient  
573 condition to obtain nonreciprocal (i.e., asymmetric) near-field radiative heat transfer between two  
574 (or more) bodies. We also note that a system with closely coupled SPPs biased by different DC  
575 currents may, under certain conditions, lead to two-stream instabilities and optical gain (negative  
576 Landau damping), as discussed in Ref. [46], potentially enabling even more opportunities for  
577 drift-biased plasmonic systems for different applications.

#### 578 4. Conclusion

579 The possibility of breaking reciprocity using a direct-current bias in conducting materials has  
580 been known for some time, but is starting to receive more attention only recently. The existing  
581 literature has been mostly focused on unidirectional propagation effects along the direction of the  
582 current and/or on specific platforms such as graphene. Here, instead, using a 3D Green function  
583 formalism and microscopic considerations, we have studied current-induced nonreciprocal  
584 effects on the entire two-dimensional surface of a generic three-dimensional plasmonic platform,  
585 elucidating the dispersion and propagation properties of nonreciprocal SPPs and revealing a  
586 number of anomalous and extreme wave-propagation effects beyond unidirectional propagation,  
587 including the possible excitation of frozen-light, steerable, surface-wave beams with enhanced  
588 and localized fields, and the presence of exceptional-point-like modal transitions at inflexion  
589 points. Since plasmonic media are inherently associated with absorption losses, we have also  
590 clarified the impact of dissipation (due to collisions and Landau damping) on nonreciprocal  
591 current-biased SPPs and the associated tradeoffs.

592 We have then focused on a particularly relevant example of application of these concepts,  
593 namely, the problem of breaking reciprocity for radiative heat transfer, which is usually achieved

594 using magneto-optical materials. We have theoretically demonstrated a signature of nonreciprocity  
595 in this context, namely, an asymmetry in the radiative heat flux density between two planar  
596 bodies for opposite in-plane wavevectors, by relying, for the first time, on a direct current bias  
597 instead of a magnetic bias. This is obtained with relatively low values of drift velocity, which  
598 could be practically realized in certain high-mobility plasmonic media, such as high-mobility  
599 semiconductors and graphene in the mid- and far-IR spectral range. Our findings in this context  
600 may suggest new possibilities and directions toward the long-sought goal of controlling radiative  
601 heat transfer without the constraints of time-reversal symmetry and reciprocity.

602 More broadly, we believe that the rich physics of drift-biased plasmonic systems, enabling  
603 nonreciprocal, slow-light, active, tunable effects at the nanoscale, may open up novel opportunities,  
604 combining the advantages of plasmonics and nonreciprocal electrodynamics, for both wave-  
605 guiding applications and thermal photonics.

## 606 Acknowledgments

607 The authors acknowledge support from the Air Force Office of Scientific Research with Grant  
608 No. FA9550-19-1-0043 through Dr. Arje Nachman and the National Science Foundation with  
609 Grant No. 1741694.

## 610 References

- 611 1. F. Monticone, "A Truly One-way Lane for Surface Plasmon Polaritons," *Nature Photonics* **14**, 461-465 (2020).
- 612 2. A. K. Zvezdin and V. A. Kotov, "Modern Magneto-optics and Magneto-optical Materials," (IOP publishing, Bristol  
613 1997).
- 614 3. Z. Wang, Y. D. Chong, J. D. Joannopoulos, M. Soljacic, "Reflectionfree One-way Edge Modes in a Gyromagnetic  
615 Photonic Crystal," *Phys. Rev. Lett.* **100**, 013905 (2008).
- 616 4. Z. Wang, Y. D. Chong, J. D. Joannopoulos, M. Soljacic, "Observation of Unidirectional Backscattering-immune  
617 Topological Electromagnetic States," *Nature* **461**, 772-775 (2009).
- 618 5. Y. Hadad, B. Z. Steinberg, "Magnetized Spiral Chains of Plasmonic Ellipsoids for One-way Optical Waveguides," *Phys.*  
619 *Rev. Lett.* **105**, 233904 (2010).
- 620 6. C. Sayrin, C. Junge, R. Mitsch, B. Albrecht, D. O'Shea, P. Schneeweiss, J. Volz, A. Rauschenbeutel, "Nanophotonic  
621 Optical Isolator Controlled by the Internal State of Cold Atoms," *Phys. Rev. X* **5**, 041036 (2015).
- 622 7. S. Ali Hassani Gangaraj and F. Monticone, "Topological Waveguiding near an Exceptional Point: Defect-Immune,  
623 Slow-Light, and Loss-Immune Propagation," *Phys. Rev. Lett.* **121**, 093901, (2018).
- 624 8. S. A. Hassani Gangaraj, F. Monticone, "Do truly Unidirectional Surface Plasmon-Polaritons Exist?," *Optica* **6**, 9,  
625 (2019).
- 626 9. M. I. Abdelrahman, and F. Monticone, "Broadband and Giant Nonreciprocity at the Subwavelength Scale in  
627 Magneto-Plasmonic Materials," *Physical Review B* **102**, 155420, (2020).
- 628 10. K. Shastri, and F. Monticone, "Dissipation-Induced Topological Transitions in Weyl Semi-Metals," *Physical Review*  
629 *Research* **2**, 033065, (2020).
- 630 11. S. A. Hassani Gangaraj, F. Monticone, "Physical Violations of the Bulk-Edge Correspondence in Topological  
631 Electromagnetics," *Phys. Rev. Lett.*, **124**, 153901, (2020).
- 632 12. S. Pakniyat, A. M. Holmes, G. W. Hanson, S. A. Hassani Gangaraj, M. Antezza, M. G. Silveirinha, S. Jam, F.  
633 Monticone, "Non-Reciprocal, Robust Surface Plasmon Polaritons on Gyrotropic Interfaces," *IEEE Trans. Antennas*  
634 *Propag.*, **68**, 5,3718-3729, (2020).
- 635 13. S. A. Hassani Gangaraj, B. Jin, C. Argyropoulos, F. Monticone, "Broadband Field Enhancement and Giant Nonlinear  
636 Effects in Terminated Unidirectional Plasmonic Waveguides," *Phys. Rev. Applied*, **14**, 054061, (2020).
- 637 14. S. A. Hassani Gangaraj, F. Monticone, "Coupled Topological Surface Modes in Gyrotropic Structures: Green's  
638 Function Analysis," *IEEE Antennas and Wireless Propagation Letters* **17**, 11, 1993-1997, (2018).
- 639 15. Z. Hayran, S. A. Hassani Gangaraj, F. Monticone, "Topologically Protected Broadband Rerouting of Propagating  
640 Waves around Complex Objects," *Nanophotonics* **8**, 8, 1371-1378 (2019).
- 641 16. K. Gallo, G. Assanto, K. R. Parameswaran, M. M. Fejer, "All-optical Diode in a Periodically Poled Lithium Niobate  
642 Waveguide," *Appl. Phys. Lett.* **79**, 314 (2001).
- 643 17. M. Soljacic, C. Luo, J. D. Joannopoulos, S. Fan, "Nonlinear Photonic Crystal Microdevices for Optical Integra-  
644 tion," *Opt. Lett.* **28**, 637 (2003).
- 645 18. I. V. Shadrivov, V. A. Fedotov, P. A. Powell, Y. S. Kivshar, N. I. Zheludev, "Electromagnetic Wave Analogue of an  
646 Electronic Diode," *New J. Phys.* **13**, 033025 (2011).
- 647 19. L. Fan, J. Wang, L. T. Varhese, H. Shen, B. Niu, Y. Xuan, A. M. Weiner, M. Qi, "An All-Silicon Passive Optical  
648 Diode," *Science* **335**, 447 (2012).

- 649 20. Y. Shi, Z. Yu, S. Fan, "Limitations of Nonlinear Optical Isolators due to Dynamic Reciprocity," *Nat. Photonics* **9**,  
650 388 (2015).
- 651 21. D. L. Sounas, J. Soric, A. Alu, "Broadband Passive Isolators Based on Coupled Nonlinear Resonances," *Nat.*  
652 *Electron.* **1**, 113 (2018).
- 653 22. Y. Fan, J. Han, Z. Wei, C. Wu, Y. Cao, X. Yu, H. Li, "Subwavelength Electromagnetic Diode: One-way Response of  
654 Cascading Nonlinear Meta-atoms," *Appl. Phys. Lett.* **98**, 151903 (2011).
- 655 23. Z. Yu S. Fan, "Complete Optical Isolation Created by Indirect Interband Photonic Transitions," *Nat. Photonics* **3**, 91  
656 (2009).
- 657 24. H. Lira, Z. Yu, S. Fan, M. Lipson, "Electrically Driven Nonreciprocity Induced by Interband Photonic Transition on  
658 a Silicon Chip," *Phys. Rev. Lett.* **109**, 033901 (2012).
- 659 25. R. Fleury, D. L. Sounas, C. F. Sieck, M. R. Haberman, A. Alu, "Sound Isolation and Giant Linear Nonreciprocity in  
660 a Compact Acoustic Circulator," *Science* **343**, 516 (2014).
- 661 26. M. Hafezi P. Rabl, "Optomechanically Induced Non-reciprocity in Microring Resonators," *Opt. Express* **20**, 7672  
662 (2012).
- 663 27. M. A. Miri, F. Ruesink, E. Verhagen, A. Alu, "Optical Nonreciprocity Based on Optomechanical Coupling," *Phys.*  
664 *Rev. Appl.* **7**, 064014 (2017).
- 665 28. N. R. Bernier, L. D. Toth, A. Koottandavida, M. A. Ioannou, D. Malz, A. Nunnenkamp, A. K. Feofanov, T. J.  
666 Kippenberg, "Nonreciprocal Reconfigurable Microwave Optomechanical Circuit," *Nat. Commun.* **8**, 604 (2017).
- 667 29. L. D. Landau, E. M. Lifshitz, L. P. Pitaevskij, "Electrodynamics of Continuous Media," 2nd ed. Elsevier: Amsterdam  
668 Vol. 8, (2008).
- 669 30. S. Fan, "Thermal Photonics and Energy Applications," *Joule* **1**, 264-273, (2017).
- 670 31. B. Zhao, G. Cheng, C. A. C. Garcia, P. Narang, S. Fan, "Axion-Field-Enabled Nonreciprocal Thermal Radiation in  
671 Weyl Semimetals," *Nano Lett.* **20**, 1923, (2020).
- 672 32. P. T. Landsberg G. Tonge, "Thermodynamic Energy Conversion Efficiencies," *J. Appl. Phys.* **51**, R1 (1980).
- 673 33. H. Ries, "Complete and Reversible Absorption of Radiation," *Appl. Phys. B* **32**, 153 (1983).
- 674 34. M. A. Green, "Time-asymmetric Photovoltaics," *Nano Lett.* **12**, 5985 (2012).
- 675 35. W. Li, S. Buddhiraju, and S. Fan, "Thermodynamic Limits for Simultaneous Energy Harvesting from the Hot Sun  
676 and Cold Outer Space," *Light Sci. Appl.* **9**, (2020).
- 677 36. P. Ben-Abdallah, "Photon Thermal Hall Effect," *Phys. Rev. Lett.* **116**, 084301 (2016).
- 678 37. L. Zhu, S. Fan, "Persistent Directional Current at Equilibrium in Nonreciprocal Many-Body Near Field Electromagnetic  
679 Heat Transfer," *Phys. Rev. Lett.* **117**, 134303, (2016).
- 680 38. L. Fan, Y. Guo, G. T. Papadakis, B. Zhao, Z. Zhao, S. Buddhiraju, M. Orenstein, S. Fan, "Nonreciprocal Radiative  
681 Heat Transfer Between Two Planar Bodies," *Phys. Rev. B* **101**, 085407, 2020.
- 682 39. L. Zhu S. Fan, "Near-complete Violation of Detailed Balance in thermal Radiation," *Phys. Rev. B* **90**, 220301(R),  
683 (2014).
- 684 40. B. Zhao, Y. Shi, J. Wang, Z. Zhao, N. Zhao, S. Fan, "Nearcomplete Violation of Kirchhoff's Law of Thermal  
685 Radiation with a 0.3 Tesla Magnetic Field," *Opt. Lett.*, **44**, 4203, (2019).
- 686 41. D. A. B. Miller, L. Zhu, S. Fan, "Universal Modal Radiation Laws for All Thermal Emitters," *Proc. Natl. Acad. Sci.*  
687 *U. S. A.* **114**, 4336-4341, (2017).
- 688 42. Y. Hadad, J. C. Soric, A. Alu, "Breaking Temporal Symmetries for Emission and Absorption," *Proc. Natl. Acad. Sci.*  
689 **113**, 3471 (2016).
- 690 43. M. Sabbaghi, H.-W. Lee, T. Stauber, K. S. Kim, "Drift-induced Modifications to the Dynamical Polarization of  
691 Graphene," *Phys. Rev. B* **92**, 195429 (2015).
- 692 44. D. S. Borgnia, T. V. Phan, L. S. Levitov, "Quasi-Relativistic Doppler Effect and Non-Reciprocal Plasmons in  
693 Graphene," arXiv: 1512.09044, (2015).
- 694 45. B. Van Duppen, A. Tomadin, A. N. Grigorenko, M. Polini, "Current-induced Birefringent Absorption and Non-  
695 reciprocal Plasmons in Graphene," *2D Mater.* **3**, 015011 (2016).
- 696 46. T. A. Morgado, M. G. Silveirinha, "Negative Landau Damping in Bilayer Graphene," *Phys. Rev. Lett.* **119**, 133901  
697 (2017).
- 698 47. K. Y. Bliokh, F. J. Fortuno, A. Y. Bekshaev, Y. S. Kivshar, F. Nori, "Electric Current Induced Unidirectional  
699 Propagation of Surface Plasmon-Polaritons," *Opt. Lett.* **43**, 963 (2018).
- 700 48. T. A. Morgado, M. G. Silveirinha, "Drift-induced Unidirectional Graphene Plasmons," *ACS Photonics* **5**, 4253,  
701 (2018).
- 702 49. T. Wenger, G. Viola, J. Kinaret, M. Fogelstrom, P. Tassin, "Current-controlled Light Scattering and Asymmetric  
703 Plasmon Propagation in Graphene," *Phys. Rev. B* **97**, 085419 (2018).
- 704 50. D. Correias-Serrano and J. S. Gomez-Diaz, "Nonreciprocal and Collimated Surface Plasmons in Drift-biased Graphene  
705 Metasurfaces," *Phys. Rev. B* **100**, 081410(R), (2019).
- 706 51. T. A. Morgado, M. G. Silveirinha, "Nonlocal Effects and Enhanced Nonreciprocity in Current-driven Graphene  
707 Systems," *Phys. Rev. B* **102**, 075102 (2020).
- 708 52. T. A. Morgado, M. G. Silveirinha, "Active Graphene Plasmonics with a Drift-current Bias," arXiv:2009.09301,  
709 (2020).
- 710 53. F. R. Prudencio, M. G. Silveirinha, "Asymmetric Electron Energy Loss in Drift-Current Biased Graphene," *Plasmonics*  
711 **16**, 19-26 (2021).

- 712 54. Y. Dong, L. Xiong, I. Y. Phinney, Z. Sun, R. Jing, A. S. McLeod, S. Zhang, S. Liu, F. L. Ruta, H. Gao, Z. Dong, R.  
713 Pan, J. H. Edgar, P. Jarillo-Herrero, L. S. Levitov, A. J. Millis, M. M. Fogler, D. A. Bandurin, D. N. Basov, "Fizeau  
714 Drag in Graphene plasmonics," *Nature* **594**, 513-516 (2021).
- 715 55. E. M. Lifshitz, L. P. Pitaevskii, "Physical Kinetics," Butterworth-Heinemann, (1981).
- 716 56. L. Novotny, B. Hecht, "Principles of Nano-Optics," Cambridge: Cambridge University Press (2006).
- 717 57. D. Svintsov and V. Ryzhii, "Comment on Negative Landau Damping in Bilayer Graphene," *Phys. Rev. Lett.* **123**,  
718 219401, (2019).
- 719 58. D. Svintsov, "Emission of Plasmons by Drifting Dirac Electrons: A Hallmark of Hydrodynamic Transport," *Phys.*  
720 *Rev. B* **100**, 195428 (2019).
- 721 59. T. A. Morgado, M. G. Silveirinha, "Morgado and Silveirinha Reply," *Phys. Rev. Lett.* **123**, 219402, (2019).
- 722 60. J. A. Bittencourt, "Fundamentals of plasma physics," 3rd ed., Springer-Verlag, (2010).
- 723 61. M.A. Miri, A. Alu, "Exceptional Points in Optics and Photonics," *Science* **363**, 7709 (2019).
- 724 62. S. A. Hassani Gangaraj, G. W. Hanson, M. G. Silveirinha, K. Shastri, M. Antezza, F. Monticone, "Unidirectional and  
725 Diffractionless Surface Plasmon Polaritons on Three-dimensional Nonreciprocal Plasmonic Platforms," *Phys. Rev. B*  
726 **99**, 245414, (2019).
- 727 63. G. W. Hanson and A. B. Yakovlev, "Investigation of Mode Interaction on Planar Dielectric Waveguides with Loss  
728 and Gain," *Radio Science*, **34**, 1349 - 1359, (1999).
- 729 64. G. W. Hanson and A. B. Yakovlev, "An analysis of Leaky-wave Dispersion Phenomena in the Vicinity of Cutoff  
730 using Complex Frequency Plane Singularities," *Radio Science*, **33**, 803 - 820, (1998).
- 731 65. A. B. Yakovlev, G. W. Hanson, "Fundamental Modal Phenomena on Isotropic and Anisotropic Planar Slab Dielectric  
732 Waveguides," *IEEE Trans. Antennas Propag.*, **51**, 888 - 897, (2003).
- 733 66. M. Y. Nada, Mohamed A. K. Othman, F. Capolino, "Theory of Coupled Resonator Optical Waveguides Exhibiting  
734 High-order Exceptional Points of Degeneracy," *Phys. Rev. B* **96**, 184304, (2017).
- 735 67. G. W. Hanson, A. B. Yakovlev, M. A. K. Othman, F. Capolino, "Exceptional Points of Degeneracy and Branch Points  
736 for Coupled Transmission Lines—Linear-Algebra and Bifurcation Theory Perspectives," *IEEE Trans. Antennas*  
737 *Propag.*, **67**, 2, (2019).
- 738 68. A. Figotin, I. Vitebskiy, "Frozen Light in Photonic Crystals with Degenerate Band Edge," *Phys. Rev. E*, **74**, 066613,  
739 (2006).
- 740 69. S. Buddhiraju, Y. Shi, A. Song, C. Wojcik, M. Minkov, I. A.D. Williamson, A. Dutt, S. Fan, "Absence of  
741 Unidirectionally Propagating Surface Plasmon-polaritons at Nonreciprocal Metal-dielectric Interfaces," *Nat.*  
742 *Commun.* **11**, 674 (2020).
- 743 70. P. Lampariello, F. Frezza, and A. A. Oliner, "The Transition Region between Bound-wave and Leaky-wave Ranges  
744 for a Partially Dielectric-loaded Open Guiding Structure," *IEEE Trans. Microwave Theory Tech.* **38**, 1831 (1990).
- 745 71. H. Shigesawa and M. Tsuji, A. A. Oliner, "The Nature of the Spectral Gap between Bound and Leaky Solutions when  
746 Dielectric Loss is Present in Printed-circuit Lines," *Radio Science* **28**, 6, 1235-1243 (1993).
- 747 72. L. Landau, E. Lifshitz, and L. Pitaevskii, "Statistical Physics," Pergamon: New York, Vol. 9, (1980).
- 748 73. G. Kirchhoff, "Ueber das Verhältniss Zwischen dem Emissionsvermögen und dem Absorptionsvermögen der Körper  
749 für Wärme und Licht," *Ann. Phys.* **185**, 275 (1860).
- 750 74. M. Planck, "The Theory of Heat Radiation," AIP-Press: New York, (1989).
- 751 75. J. R. Howell, M. P. Menguuc, R. Siegel, "Thermal Radiation Heat Transfer," 6th ed.; CRC Press: London, (2016).